# A Appendix

## A.1 Conversion of properties and units

In the literature various units are used for the energy and the magnetic properties. In table A.1 the conversion of energy units is given. For the purpose of converting surface and volume anisotropy energy densities table A.2 can be utilized. The units of the most important magnetic properties can be converted as follows:

Magnetic field strength : $H[\text{Oe}] \cdot 79.58 = H[\text{A/m}]$

Magnetic flux density: $B[\text{G}] \cdot 10^{-4} = B[\text{T}]$

Magnetization: $4\pi M[\text{G}] \cdot 79.58 = M[\text{A/m}]$ or $M[\text{G}] = M[\text{kA/m}]$

**Table A.1:** Conversion of energy units.

| | J | erg | eV |
|---|---|---|---|
| 1 J | 1 | $10^{7}$ | $6.242 \cdot 10^{18}$ |
| 1 erg | $10^{-7}$ | 1 | $6.242 \cdot 10^{11}$ |
| 1 eV | $1.602 \cdot 10^{-19}$ | $1.602 \cdot 10^{-12}$ | 1 |

**Table A.2:** Lattice constants, surface and volume density of atoms and proportionality constants for the conversion of erg cm$^{-2}$ (1 mJ m$^{-2}$) and $10^{6}$ erg cm$^{-3}$ ($10^{5}$ J m$^{-3}$) to $\mu$eV/atom.

| | Lattice constant (nm) | Atoms cm$^{-2}$ | 1 erg cm$^{-2}$ multiplied by | Atom cm$^{-3}$ | $10^{6}$ erg cm$^{-3}$ multiplied by |
|---|---|---|---|---|---|
| fcc Ni(100) | 0.352 | $1.61 \cdot 10^{15}$ | 386 $\mu$eV/atom | $9.17 \cdot 10^{22}$ | 6.83 $\mu$eV/atom |
| fct Ni(Fe) /Cu(100) | 0.361 | $1.78 \cdot 10^{15}$ | 350 $\mu$eV/atom | $9.03 \cdot 10^{22}$ | 6.91 $\mu$eV/atom |
| fcc Fe(100) | 0.359 | $1.55 \cdot 10^{15}$ | 403 $\mu$eV/atom | $8.65 \cdot 10^{22}$ | 7.22 $\mu$eV/atom |
| bcc Fe(100) | 0.286 | $1.21 \cdot 10^{15}$ | 515 $\mu$eV/atom | $8.46 \cdot 10^{22}$ | 7.38 $\mu$eV/atom |

## A.2 Drawings of the UHV-components

In table A.3 the position of the flanges of the UHV-chamber and the respective applications are listed. The flanges are numbered and can be found in the different views of the UHV-chamber shown in Fig. A.1. In the following drawings of the sample holder, the $\mu$-metal shielding, the SQUID holder and the UHV-cryostat are presented with their dimensions.

**Table A.3:** Construction of the UHV-chamber: positions of the flanges and the respective applications.

| No. of flange | Type | Application | Azimuthal angle (°) | Polar angle (°) | Length (mm) | Tube $\varnothing_i$ (mm) | Shift (mm) |
|---|---|---|---|---|---|---|---|
| 1 | DN 100 CF | CMA | 90 | 90 | 381 | 104 | - |
| 2 | DN 100 CF | Manipulator | 180 | 90 | 228 | 100 | - |
| 3 | DN 160 CF | LEED | 270 | 90 | 224 | 150 | - |
| 4 | DN 100 CF | Glass finger | 0 | 90 | 262 | 150 | - |
| 5 | DN 63 CF | SQUID | - | 0 | 180 | 66 | - |
| 6 | DN 160 CF | Pumps | 240 | 90 | 160 | 146 | z=-180 |
| 7 | DN 63 CF | Plasmasource | 135 | 145 | 252 | 66 | - |
| 8 | DN 160 CF | Evaporators | - | 180 | 302 | 150 | - |
| 9 | DN 16 CF | View port | 0 | 35 | 150 | 16 | - |
| 10 | DN 40 CF | View port | - | 0 | 133 | 38 | x=174 |
| 11 | DN 16 CF | Spare | 90 | 72 | 110 | 16 | x=174 |
| 12 | DN 16 CF | Spare | 270 | 72 | 110 | 16 | x=174 |
| 13 | DN 16 CF | Spare | 90 | 40 | 110 | 16 | x=174 |
| 14 | DN 16 CF | Spare | 270 | 40 | 110 | 16 | x=174 |
| 15 | DN 40 CF | Ion gauge | 90 | 90 | 117 | 38 | x=-170 |
| 16 | DN 63 CF | View port | 160 | 50 | 176 | 66 | - |
| 17 | DN 40 CF | Sputter gun | 225 | 45 | 140 | 38 | - |
| 18 | DN 40 CF | View port | 270 | 60 | 131 | 38 | x=110 |
| 19 | DN 40 CF | View port | 90 | 90 | 135 | 38 | z=-94 |
| 20 | DN 40 CF | QMS | 45 | 40 | 184 | 38 | - |
| 21 | DN 16 CF | View port | 45 | 100 | 164 | 16 | - |
| 22 | DN 16 CF | View port | 225 | 100 | 164 | 16 | - |
| 23 | DN 16 CF | Spare | 270 | 90 | 113 | 16 | x=132 |
| 24 | DN 16 CF | Aperture plate | 90 | 90 | 113 | 16 | x=-94 |
| 25 | DN 16 CF | View port | 90 | 40 | 140 | 16 | - |

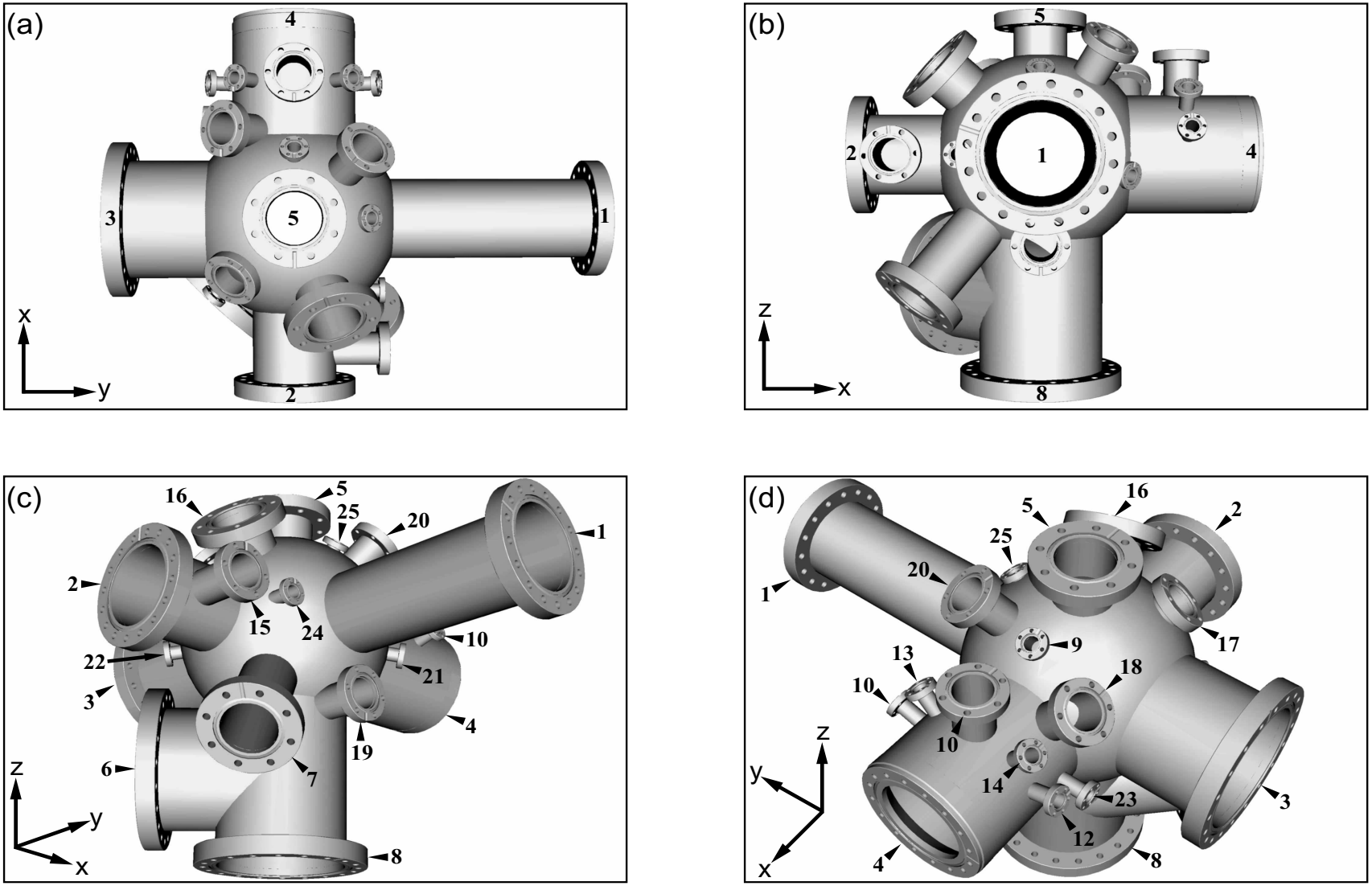


**Figure A.1:** Different views of the UHV-chamber: (a) top view , side view (b) and two 3D-views (c,d). The dimensions and angles of the numbered flanges and their applications are described in table A.3.

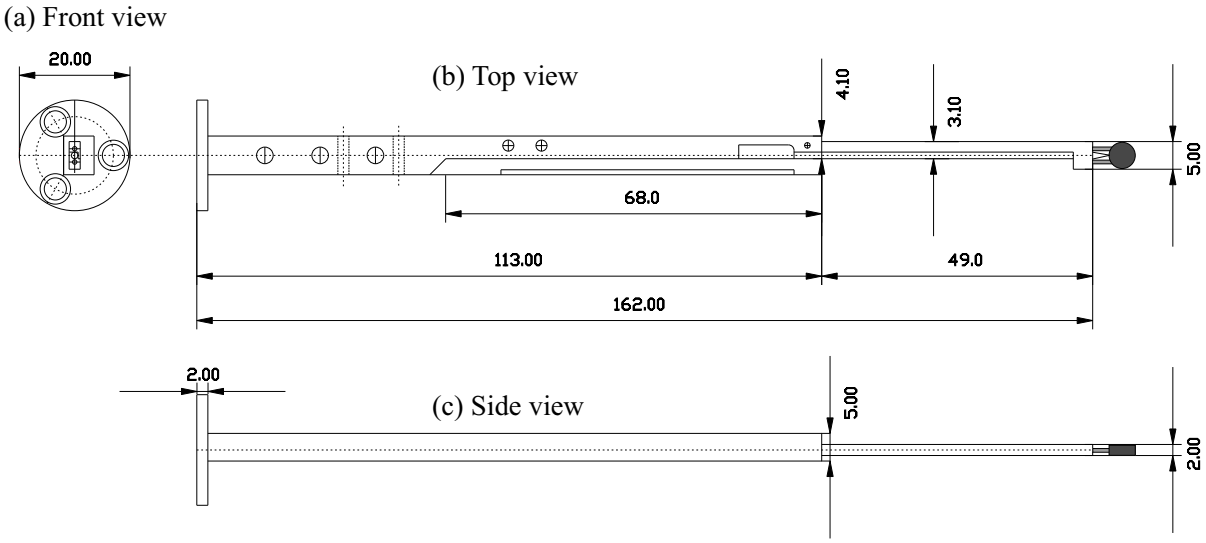


**Figure A.2:** Dimensions in mm and different views of the sample holder made of oxygen-free copper, which is connected to the lHe-cooled manipulator via a sapphire plate at the left end. The substrate is held by a tungsten wire of 0.3 mm thickness for resistive heating, guided by two ceramic tubes of 0.8 mm outer diameter (gray) which stabilize the crystal (dark gray). The substrate can easily be exchanged.

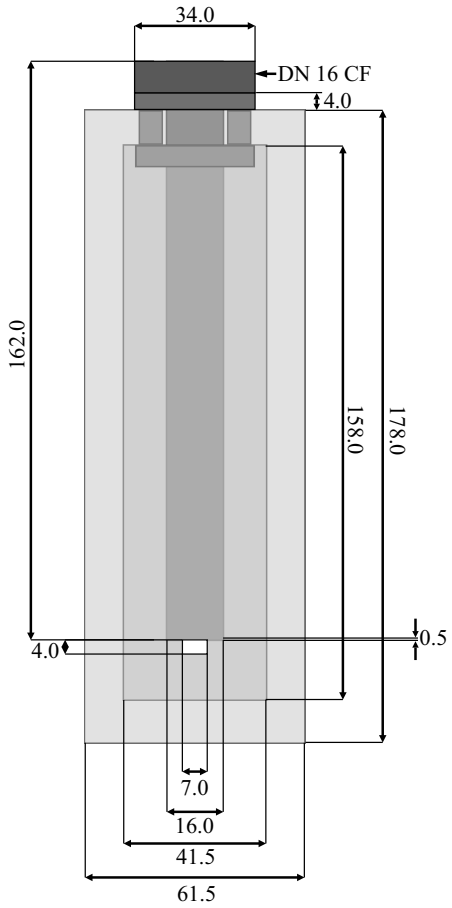


**Figure A.3:** Dimensions in mm of the cryostat finger and the surrounding $\mu$-metal screening. The cryostat finger (dark gray) is made of non-magnetic steel (1.4301) and is welded to a DN 16 CF flange at the upper part which is connected to the main cryostat. The $\mu$-metal shielding is constructed of two cylinders of 0.7 mm wall thickness. All components are screwed together. Through the rectangular slit of $4 \times 7$ mm$^2$ (white) the sample is moved into the screening. The calculated screening factor of this setup is $7 \times 10^3$ and $7 \times 10^5$ along and perpendicular to the vertical axis, respectively.

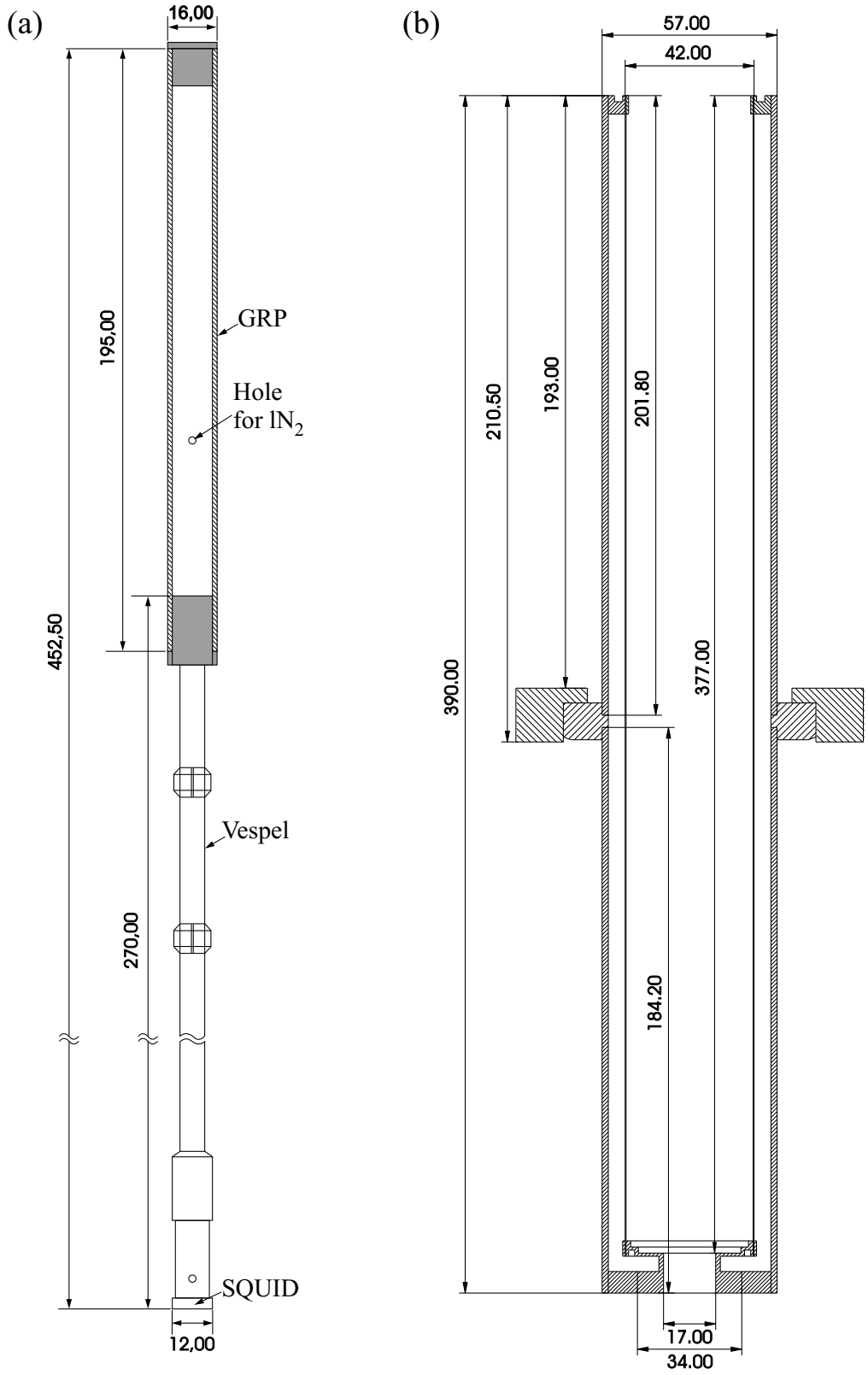


**Figure A.4:** (a) Dimensions in mm of the SQUID holder made of a *Vespel* rod, which is connected to a tube of glass fiber reinforced plastic (GRP). (b) Dimensions in mm of the cryostat mounted on a DN 63 CF flange.

## A.3 Motor control and data acquisition program

The main program controls the two stepper motors which transfer and rotate the manipulator, in order to position the sample with respect to the desired application. It was developed by F. Römer and is based on *LabView 6.1*. Due to its voluminous structure the wiring diagram has not been printed here. With the control panel shown in Fig. A.5 the sample position can directly be approached by setting the angle of rotation $\theta$ and the transfer distance $x$. Once the angle $\theta$ is calibrated to the position of the respective application, the sample can be moved at the push of a button in the upper left corner of the control panel. Alternatively, $\theta$ can be adjusted by the large turning knob on the left hand side or the input field below it. The current


**Figure A.5:** Control panel of the main program, which allows for specific sample manipulation. Rotation and horizontal translation are governed and displayed by the turning knobs and the control slides, respectively. Sample positions for the various investigation techniques can be individually calibrated, saved and retrieved. The button “SQUID Control” grants access to the SQUID data acquisition program displayed in Fig. A.6.

angle is then displayed by the large turning knob on the right hand side and the output field below it. Analogously, the new horizontal $x$-position can be either set by the control slide or the input field in the middle of the panel. Again, a previously performed calibration of the $x$-position allows for a quick approach of the desired device. The current $x$-position is displayed by the upper control slide and the output field above it. Moreover, on the lower right hand side different modi of the velocity for the movement of the manipulator can be chosen. If the button *Jog Control* is pushed the manipulator can be operated by remote control. For SQUID measurements a subprogram can be started by pushing the button *SQUID Control* at the bottom of the main control panel. The SQUID control panel is depicted in Fig. A.6. It is divided into the graph, which displays the SQUID output voltage –proportional to the stray field component $B_z$ of the sample– versus the $x$-position, and the fields for setting the parameters. The stray field distribution can be observed either during or after (*Liveshow OFF*) the measurement. Having chosen the direction of movement along the $x$-axis by the lever below the graph, measurements are started by the accordingly labelled knob on the right hand side and can be saved either manually or automatically (*Autosave ON*). Before a measurement the data acquisition can be specified by choosing the number of output values to be averaged per measuring point (*Scans*

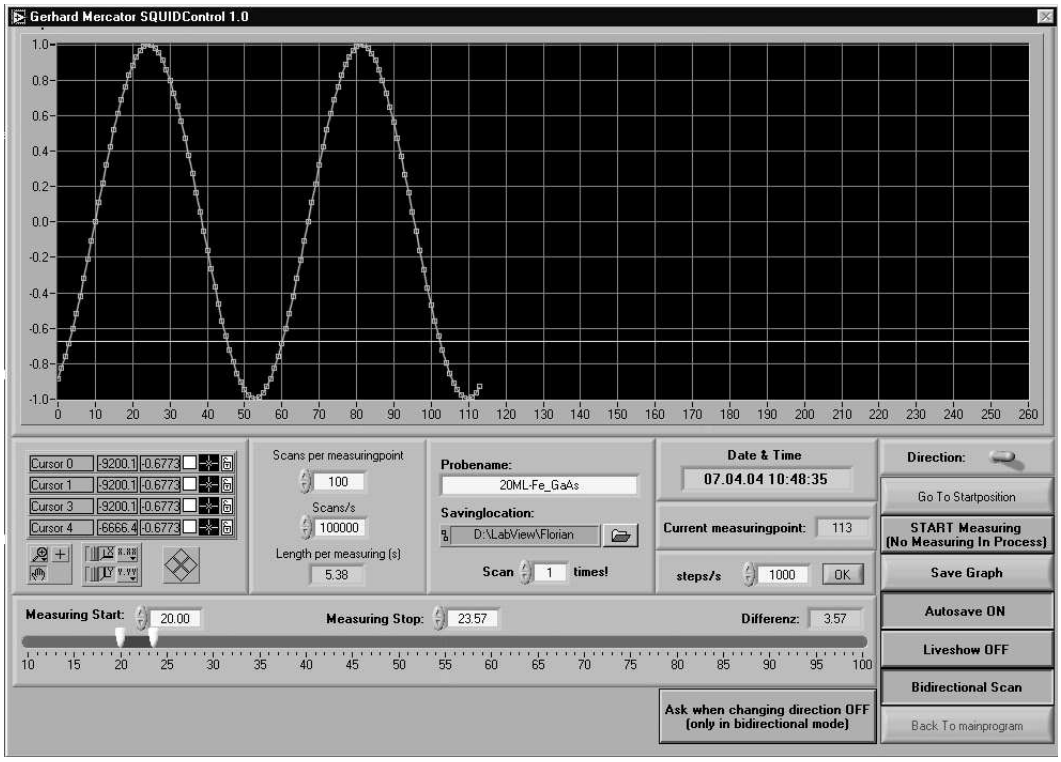


**Figure A.6:** Control panel of the program, which allows for SQUID data acquisition. An $x$-$y$-chart displays the SQUID signal versus the $x$-position (here a test pattern is shown). Start and end position of the scan as well as the velocity, the direction, the number of repetitions and file name of the measurement can be chosen. In the auto-save mode every scan is saved automatically.

*per measuring point*). Furthermore, the data acquisition per second (*Scan/s*) at the input unit can be defined, which in combination with the scans per measuring point determines the total duration of acquisition per point. The total period of one measurement is output in the field *Length of measuring (s)*, which is determined by the totally covered distance adjusted by the control slide at the bottom and the velocity of the motor.

## A.4 Technical data of the SQUID sensor

**Table A.4:** Technical details of the SQUID. From [200].

| | |
|---|---|
| Manufacturer | Jülicher SQUID GmbH |
| Washer | $\varnothing = 3.5$ mm |
| SQUID-Loop | $100 \times 100$ $\mu$m$^2$ |
| Inductance | 260 pH |
| Tank circuit | Lumped element |
| Resonance frequency | 861 MHz |
| Coupling (rf absorption) | $-26$ dB |
| Quality factor | 340 |
| SQUID signal amplitude | 0.5 $V_{pp}$ |
| Resolution | $<1$ pT/$\sqrt{\text{Hz}}$ |
| Transfer coefficient | $0.64(1)$ V/$\Phi_0$ |
| Intrinsic calibration | 9.3 nT/$\Phi_0$ |

## A.5 Calibration of the Fe evaporator

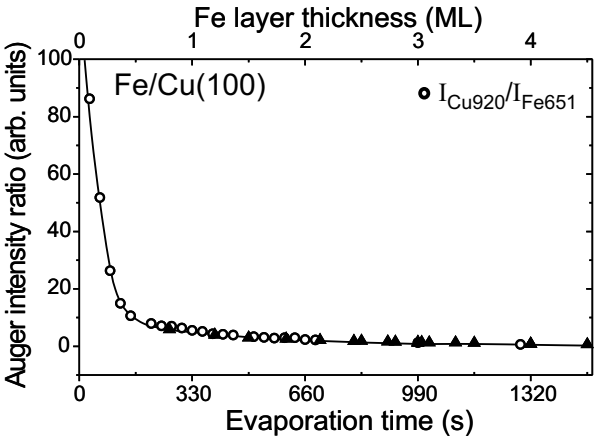


**Figure A.7:** Calibration of the Fe evaporator by the ratio of the Auger peak intensities $Cu_{920}$ and $Fe_{651}$ of various Fe/Cu(100) spectra as a function of the evaporation time and the corresponding Fe layer thickness (circles). The triangles represent earlier measurements [175]. The curve is a guide to the eye.

## A.6 Determination of the canting angle from XMCD measurements

The relevant lengths shown in Fig. A.8 are given by:

$$\overline{OW} = M_{||}\sin(\theta) \tag{A.1}$$

$$\overline{OV} = M_{||}\cos(\theta) \tag{A.2}$$

$$\overline{OZ} = \frac{M_{||}}{\cos(\theta)} \tag{A.3}$$

$\theta$ being the angle of incidence of the x-ray beam. By using the theorem on intersecting lines, $x$ from Fig. A.8 is given by:

$$x = (\overline{OZ} - M_{\perp}) \times \frac{\overline{OW}}{\overline{OZ} - \overline{OV}} \tag{A.4}$$

The canting angle $\alpha$ of the magnetization is defined by:

$$\tan(\alpha) = \frac{x}{M_{\perp}} \tag{A.5}$$

$$\tag{A.6}$$

The computation yields:

$$\alpha = \arctan\Big(\frac{M_{||} - M_{\perp}\cos(\theta)}{M_{\perp}\sin(\theta)}\Big) \tag{A.7}$$

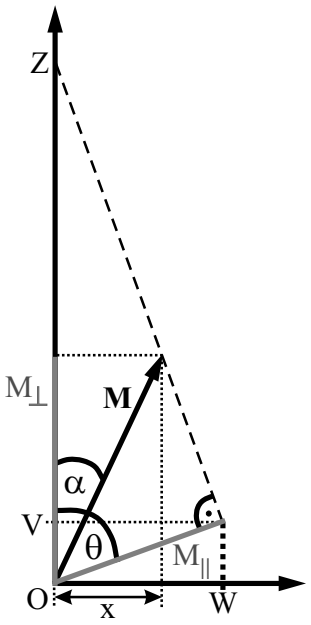


**Figure A.8:** Determination of the canting angle $\alpha$ of the magnetization $\mathbf{M}$ by using the theorem on intersecting lines. $M_{\perp}$ and $M_{||}$ are the projections of $\mathbf{M}$ onto the directions of the incident x-ray, whereas $x$ is the true in-plane component of $\mathbf{M}$.

Since the measured XMCD intensities $I_{\perp}$ and $I_{||}$ are proportional to the respective components of $\mathbf{M}$, the canting angle of the magnetization can be obtained from:

$$\alpha \;=\; \arctan\Big(\frac{I_{||} - I_{\perp}\cos(\theta)}{I_{\perp}\sin(\theta)}\Big) \tag{A.8}$$